AUT Journal of Mechanical Engineering

AUT J. Mech. Eng., 2(1) (2018) 27-38
DOI: 10.22060/mej.2017.13172.5561

Influence of Burner Head Design on Its Thermal and Environmental Characteristics

S. F. Mousavi Kolousforoushi, J. Mahmoudimehr*

Faculty of Mechanical Engineering, University of Guilan, Rasht, Iran

ABSTRACT: In this paper, for the first time, four thermal and environmental objective functions are simultaneously taken into account in the process of the optimal design of a natural gas diffusion burner. The burner thermal efficiency and the emissions of carbon monoxide, nitrogen oxide, and unburned methane constitute the objective functions of the present study. In the first step, the burner is numerically simulated, and the simulation results are verified through being compared with the available experimental data. Next, the simulation is carried out for the different set values of design variables (the dimensions of the air and fuel inlets, and the overall equivalence ratio) and the optimum design is chosen by using "Pareto front concept". The paper will show that as a result of the mentioned procedure, the burner thermal efficiency is increased by 29.4%, and the emissions of carbon monoxide, nitrogen oxide, and unburned methane are decreased by 81.2%, 98.6%, and 83.9%, respectively. The manuscript explains the reasoning for the superiority of the modified design over the reference one in detail.

Review History:
Received: 23 July 2017
Revised: 18 October 2017
Accepted: 30 October 2017
Available Online: 1 December 2017

Keywords:
Diffusion burner
Numerical modeling
Multi-objective design
Thermal efficiency
Pollutants

1- Introduction

The IEA reported that 81.1% of the world total primary energy demand was supplied from the combustion of fossil fuels in 2014 [1]. This high level of usage can lead to the depletion of fossil fuel resources in the coming decades; moreover, it made the fossil fuels the major cause of environmental pollution [2]. Consequently, it is very important to improve the combustion efficiency in order to minimize both fuel consumption and the emission of pollutants. In this regard, various research works have been focused on the burner head design along with its overall equivalence ratio (OER).

Papanikolaou and Wierzba [3] experimentally studied the influence of nozzle geometry (circular or elliptic) on the stability limits of a jet diffusion flame issuing into a co-flowing air stream. The results indicated that only attached flames, but not lifted flames, are influenced by the nozzle geometry. For an inverse diffusion flame (IDF), Sobiesiak and Wenzell [4] experimentally showed that fuel/air nozzle diameter ratio and fuel to air OER could be optimized to produce an extended region of uniform and high temperature. Sze et al. [5] experimentally compared two IDFs, one with circumferentially arranged ports (CAP) and the other with co-axial (COA) jets. The results showed that at low OERs, the temperature distributions of the CAP and COA flames were similar; however, at higher OERs, the peak temperature of the CAP flame was higher than that of the COA flame. It was also observed that there was more intense air–fuel mixing in a CAP flame than the COA one. Experimental study of Hariharan et al. [6] showed that the premixed flame of an elliptic nozzle was longer, had a lower liftoff velocity, radiated less, produced higher peak temperatures, and had a lower peak NO as compared to the flame of a circular nozzle. Furthermore, it was observed that global NO decreased by increasing air to fuel OER for both nozzle shapes. Four types of burner head configurations (radial flow, swirling flow, vertical flow, and porous radiant) were experimentally tested by Makmool et al. [7]. The results indicated that, among the tested burners, the swirling flow burner led to the highest thermal efficiency. Moreover, it was observed that despite its low CO emission, the conventional radial flow burner was not attractive for household use due to its inefficient utilization of the energy. Liu and Smallwood [8] modified a conventional co-flow diffusion flame burner by introducing a central air jet inside the fuel tube. The numerical and experimental evaluations indicated that the mentioned modification was an effective means to control the flame size, structure, and sooting characteristics. An IDF with a central air jet surrounded by an array of fuel jets for the impingement heating was experimentally studied by Dong et al. ([9,10]). The results showed that smaller air nozzle diameter produced a blue flame with better thermal characteristics, higher maximum flame temperature, higher heat flux, wider range of flame stability, and wider operation range of OER. Moreover, the smaller air nozzle diameter produced more incomplete combustion products of CO and HC but less NO, which was attributed to the lower volume of high-temperature zone and shorter flame residence time. Dong et al. [11] experimentally studied the effects of OER and air inlet diameter on the thermal efficiency of an impinging IDF. The results showed that the maximum thermal efficiency was obtained when the flame reaction zone directly impinged on the plate under quasi-stoichiometric conditions; moreover, thermal efficiency decreased as the air jet diameter increased. Zhen et al. [12] experimentally investigated the effects of nozzle

Corresponding author, E–mail: mahmoudimehr@guilan.ac.ir

length on the thermal and environmental characteristics of a multi-fuel-jet IDF. The results showed that a shorter nozzle produced a flame with a shorter base height and a smaller potential core due to the enhanced air/fuel mixing. Moreover, it led to a faster and more complete combustion at the inner reaction core of the flame as well as higher peak values of CO and CO2 concentrations. Kashkousha et al. [13] numerically and experimentally studied the characteristics of concentric elliptical jet diffusion flames for pollution (NO and HC) reduction and more flexible firing. The results showed that the optimum relative angular positioning of the air and fuel jets depended on the co-flow velocity and aspect ratio. Mahesh and Mishra [14] experimentally studied the effects of the recession of the central air jet on the flame properties of a coaxial diffusion burner. The observations revealed a negligible reduction in the flame height by increasing the recession of the air jet. Moreover, the results showed a reduction in the luminosity of the flame by increasing air jet recession for Reynolds number (Re) of 3421. In another numerical and experimental work, Mahesh and Mishra [15] showed that un-recessed IDF had a higher flame stability as compared to the recessed case for the same fuel jet velocity.
Lamige et al. [16] experimentally showed that fuel nozzle lip thickness strongly affected the stability limits of an attached flame through creating a wake flow behind the nozzle rim. The experimental investigations of Zhen et al. [17] revealed an improvement in the thermal efficiency and some reductions in the emissions of a domestic gas stove burner as a result of redesigning the burner cap to utilize the swirl flows. The empirical study of Saediamiri et al. [18] indicated that the fuel nozzle geometry had great impacts on the stability limits of non-premixed lifted biogas flame. These findings revealed that the blow-out velocity of a smaller diameter nozzle was higher than that of a larger one. Akbarzadeh and Birouk [19] conducted an experimental study on the effect of the circular and rectangular fuel nozzle orifice geometry on the stability of a turbulent non-premixed methane flame. Results showed that a circular nozzle could improve the stability of the turbulent non-premixed methane flame by accelerating the liftoff of an attached flame and decreasing the liftoff height. Saediamiri et al. [20] examined the effect of the fuel nozzle geometry on the stability limits of a low swirl non-premixed biogas flame. Fuel nozzle geometry was changed by changing its diameter or the number of circumferential holes, while the total cross-sectional area was kept constant. The results revealed that the swirl was essential for stabilizing a turbulent non-premixed biogas lifted flame. More importantly, the fuel nozzle was found to drastically influence both the attached and lifted biogas flame stability limits. Kuntikana and Prabhu [21] presented experimental and numerical investigations on the influence of the equivalence ratio and the burner to plate spacing on the thermal characteristics of inline and staggered configurations of a multi-port plate methane-air premixed burner. In the staggered configuration, the heat flux uniformity was assured due to the biased arrangement. The increase in the mixture flow improved the heat transfer and the increase in the burner to plate spacing lowered the thermal efficiency due to a higher ambient air entrainment.
The analysis of combustion processes was limited to the measurements and observations prior to the development of computer simulation software. Nowadays, computer simulation is indispensable for the analysis and improvement of reacting flow systems [22]. This paper employs numerical simulation, which is verified through being compared with available experimental data, to improve the thermal and environmental characteristics of a confined natural gas diffusion flame through the examination of the various settings of the design parameters (the sizes of fuel and air inlets, and the OER). The contributions of the present paper to the subject are as follows:

- To the best of authors' knowledge, it is the first time that four thermal and environmental objective functions (burner thermal efficiency, and the emissions of CO, NO, and unburned CH4) are simultaneously taken into account to achieve an optimum burner design
- The paper presents a series of superior designs (on the basis of Pareto front concept) each of which may be considered as the optimal design, depending on the designer's priorities
- The paper reaches a modified burner design with great improvements in the mentioned objective functions

2- Theoretical Modeling

2- 1- Governing equations

In this study, a simplified two-step mechanism is considered for the combustion of methane as shown in Eq. (1) [23]:

$$\begin{aligned} &CH_4 + \frac{3}{2}O_2 \rightarrow CO + 2H_2O \\ &CO + \frac{1}{2}O_2 \rightarrow CO_2 \end{aligned} \tag{1}$$

The governing partial differential equations for the steady reacting flow are listed below.
Continuity [24]:

$$\frac{\partial}{\partial x_i}\left(\rho u_i\right) = 0 \tag{2}$$

Momentum [24]:

$$\begin{aligned} &\frac{\partial}{\partial x_j}\left(\rho u_i u_j\right) = -\frac{\partial p}{\partial x_i} \\ &+\frac{\partial}{\partial x_j}\left[\mu\left(\frac{\partial u_i}{\partial x_j}+\frac{\partial u_j}{\partial x_i}-\frac{2}{3}\delta_{ij}\frac{\partial u_l}{\partial x_l}\right)\right]+\frac{\partial}{\partial x_j}\left(-\rho\overline{u_i' u_j'}\right) \end{aligned} \tag{3}$$

In this study, the fluctuating term (the last term on the right-hand side) is modeled using the standard k-ϵ turbulence model ([24]).
Species balance [23]:

$$\frac{\partial}{\partial x_i}\left(\rho u_i Y_k\right) = \frac{\partial}{\partial x_i}\left(\left(\rho D_k + \frac{\mu_t}{\mathrm{Sc}_t}\right)\frac{\partial Y_k}{\partial x_i}\right) + R_k \tag{4}$$

$$R_k = M_{w.k}\sum_{r=1}^{N_R} R_{k.r} \tag{5}$$

In this study, the molar rate of creation/destruction of species k in reaction r (R_k,r) is determined by the hybrid Arrhenius-

eddy dissipation model on the basis of which the reaction rate is limited by the slower mechanism between turbulence mixing and chemical kinetics. In this model, both the Arrhenius rate (Eq. (6)) and the eddy-dissipation rate (Eqs. (7) and (8)) are calculated. The net reaction rate is then taken as the minimum of these rates [25].

$$R_{k,r} = A_r T^{\beta} e^{\frac{-E}{RT}} \tag{6}$$

$$R_{k,r} = \nu'_{k.r} M_{w.k} A \rho \frac{\varepsilon}{k} \min\left(\frac{Y_R}{\nu'_{R.r} M_{w.R}}\right) \tag{7}$$

$$R_{\mathrm{k,r}} = \nu'_{\mathrm{k.r}} M_{\mathrm{w.k}} \mathrm{A\,B}\, \rho \frac{\varepsilon}{k} \frac{\sum_{\mathrm{P}} Y_{\mathrm{P}}}{\sum_{\mathrm{j}}^{N} \nu''_{\mathrm{j.r}} M_{\mathrm{w.j}}} \tag{8}$$

Radiation [26]:

$$\frac{\mathrm{d}I(\vec{r}.\vec{s})}{\mathrm{d}s} + (a+\sigma_{\mathrm{s}})\mathrm{I}(\vec{r}.\vec{s}) = an^2 \frac{\sigma T^4}{\pi} + \frac{\sigma_{\mathrm{s}}}{4\pi} \int_0^{4\pi} I(\vec{r}.\vec{s}') \,\mathrm{d}\Omega' \tag{9}$$

Where the local absorption coefficient (a) is obtained from the weighted sum of gray gases model (WSGGM) ([26]). Moreover, the radiation heat source is obtained from Eq. (10), where A denotes the surface of each cell.

$$S_{\mathrm{h.radiation}} = \int_A \left(\int I\vec{s}.\vec{n}\,\mathrm{d}\Omega'\right)\mathrm{d}A \tag{10}$$

In the present work, the radiation heat transfer is modeled by using Discrete Ordinates (DO) model ([27]). In this model, Eq. (9) is solved for a sufficient number of discrete directions determined through solution independency analysis.

Energy [23]:

$$\frac{\partial}{\partial x_{\mathrm{i}}}(\rho u_{\mathrm{i}} h) = \frac{\partial}{\partial x_{\mathrm{i}}}\left(\left(k + \frac{c_{\mathrm{p}}\mu_{\mathrm{t}}}{\mathrm{Pr}_{\mathrm{t}}}\right)\frac{\partial T}{\partial x_{\mathrm{i}}}\right) + \frac{\partial}{\partial x_{\mathrm{i}}}\left(\sum_{\mathrm{k}} h_{\mathrm{k}}\left(\rho D_{\mathrm{k}} + \frac{\mu_{\mathrm{t}}}{\mathrm{Sc}_{\mathrm{t}}}\right)\frac{\partial Y_{\mathrm{k}}}{\partial x_{\mathrm{i}}}\right) + S_{\mathrm{h.Reaction}} + S_{\mathrm{h.Radiation}} \tag{11}$$

In the energy equation, the reaction heat source is calculated as shown in Eq. (12).

$$S_{\mathrm{h.Reaction}} = -\sum \frac{h_{\mathrm{k}}^0}{M_{\mathrm{w.k}}} R_{\mathrm{k}} \tag{12}$$

NO transport [28]:

$$\nabla.(\rho\vec{u}Y_{\mathrm{NO}}) = \nabla.(\rho D \nabla Y_{\mathrm{NO}}) + S_{\mathrm{NO.Thermal}} + S_{\mathrm{NO.Prompt}} \tag{13}$$

In this work, no formation is assumed to be governed by the Zeldovich (thermal) and Fenimore (prompt) mechanisms. These mechanisms are important at high temperatures and fuel-rich conditions, respectively. Thermal and prompt NO (Nitrogen Oxide) source terms are approximated by Eqs. (14) and (15), respectively [28].

$$S_{\mathrm{NO.Thermal}} = 2k_{\mathrm{f.1}}[\mathrm{O}][\mathrm{N_2}] \frac{\left(1 - \frac{k_{\mathrm{r.1}}k_{\mathrm{r.2}}[\mathrm{NO}]^2}{k_{\mathrm{f.1}}[\mathrm{N_2}]k_{\mathrm{f.2}}[\mathrm{O_2}]}\right)}{\left(1 + \frac{k_{\mathrm{r.1}}[\mathrm{NO}]}{k_{\mathrm{f.2}}[\mathrm{O_2}] + k_{\mathrm{f.3}}[\mathrm{OH}]}\right)} \tag{14}$$

$$S_{\mathrm{NO.Prompt}} = f\,[\mathrm{O_2}]^g[\mathrm{N_2}][\mathrm{fuel}]\exp\left(-\frac{E'_{\mathrm{d}}}{RT}\right) \tag{15}$$

In the present work, the above-mentioned equations are solved with the finite volume approach by using Fluent© software. Also, the mesh generation is carried out by using Gambit software. Second-order upwind scheme and SIMPLE algorithm are used for the discretization of the governing equations and the pressure-velocity coupling, respectively ([29]).

2- 2- Modeling verification

To verify the present modeling, the simulation results are compared to the experimental data ([30]) available for the axial-symmetric case study schematically shown in Fig. 1. The specifications of the air and fuel streams are presented in Table 1. Mass flow inlet is considered as the boundary condition of both the air and fuel inlets. Combustion chamber walls are assumed to have no-slip condition, to be fixed at 393.15K, and to have the emissivity factor of 0.6. The outlet pressure is fixed at 1atm, and the axisymmetric boundary condition is applied to the chamber centerline. The convergence criteria for the different governing equations are listed in Table 2. Fig. 2 shows the mesh independency analysis on the basis of the flow temperature on the centerline. Regarding Fig.2, a 22000-quadrilateral-cell structured mesh (88 ×250) was considered to be sufficiently fine, since a finer mesh did not lead to a noticeable change. Fig. 3 shows an acceptable agreement (with an average difference of <10%) between the numerical results and the experimental data for the flow temperature and the mass fraction of CH_4 on the centerline.

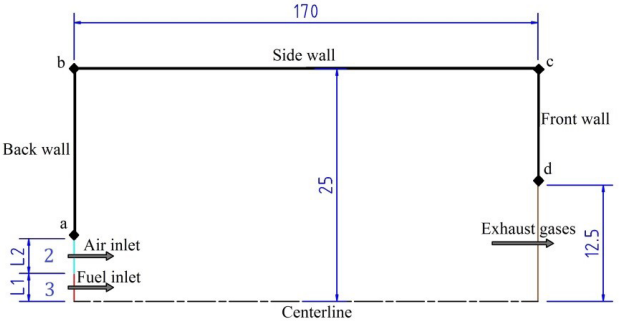

Fig. 1. Burner geometry (dimensions are in cm)

Table 1. Air and fuel streams data

Parameter	At fuel inlet	At air inlet
Mass flow rate, kg/s	0.0125	0.186
Velocity, m/s	7.76	36.29
Temperature, K	313.15	323.15
Oxygen mass fraction	0	0.23
Nitrogen mass fraction	0.1	0.76
Methane mass fraction	0.9	0
Water mass fraction	0	0.01

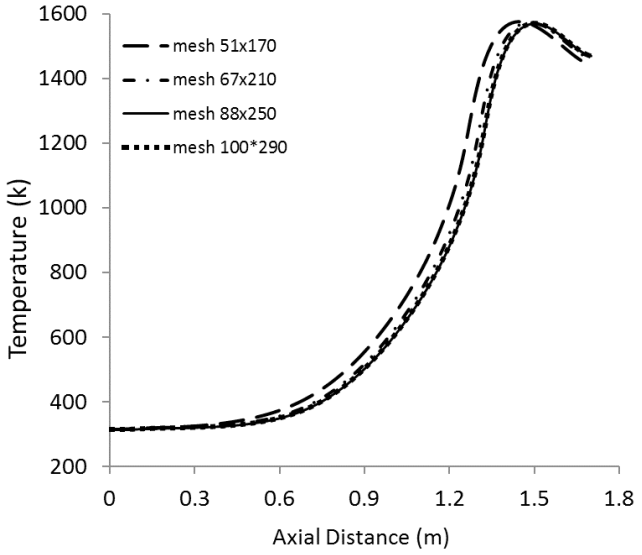

Fig. 2. Mesh independency analysis on the basis of the flow temperature on the centerline

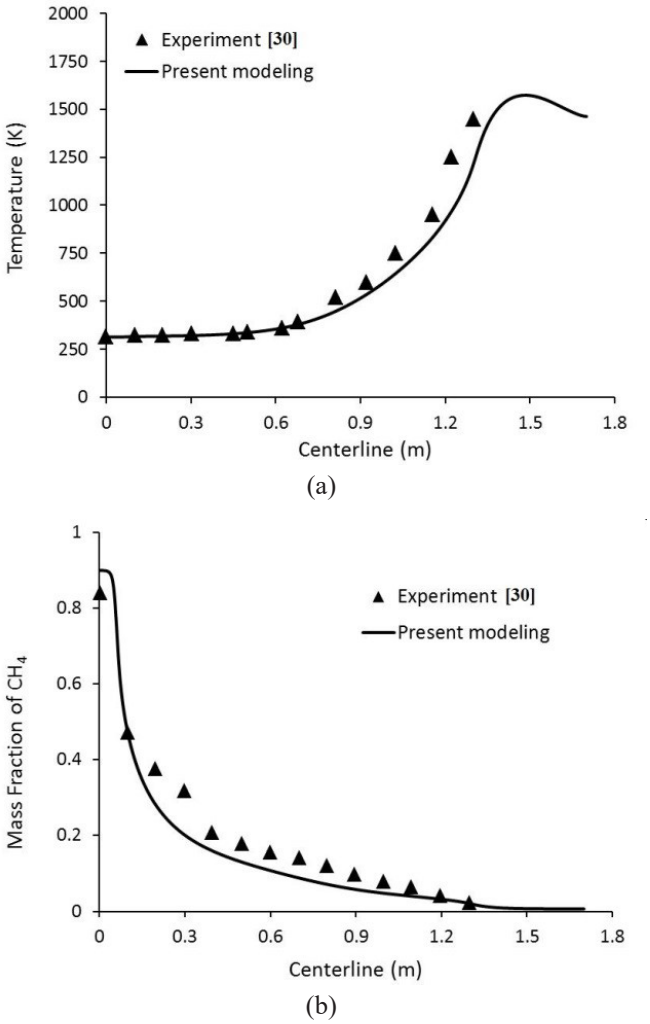

Fig. 3. Comparison of the numerical and experimental data for (a) temperature (b) methane mass fraction on the centerline

3- The Optimization Problem and Pareto Front Concept

Objective functions and design variables along with their domains of change are presented below:

Objective functions:

- 1st Objective function: Maximize thermal efficiency ; $\eta(L_1, L_2, \phi)$
- 2nd Objective function: Minimize Emission of CO ; $CO(L_1, L_2, \phi)$
- 3rd Objective function: Minimize Emission of NO; $NO(L_1, L_2, \phi)$
- 4th Objective function: Minimize Emission of unburned CH_4 ; $CH_4(L_1, L_2, \phi)$

Design variables:

- 1st design variable: Dimension of fuel inlet; L_1, cm {2, 2.5, 3, 3.5, 4}
- 2nd design variable: Dimension of air inlet; L_2 , cm {1, 1.5, 2, 2.5, 3, 3.5, 4}
- 3rd design variable: Air to fuel overall equivalence ratio; Φ {0.95, 1, 1.1, 1.2, 1.3}

In this study, while the fuel mass flow rate is constrained to be constant, it is attempted to reach a better thermal and environmental characteristics of a flame through the examination of the different settings of the above-described design variables. In this regard, five different values (0.95, 1, 1.1, 1.2, and 1.3) are considered for air to fuel OER, five different values (2cm, 2.5cm, 3cm, 3.5cm, and 4cm) are considered for L_1, and seven different values (1cm, 1.5cm, 2cm, 2.5cm, 3cm, 3.5cm and 4cm) are considered for L_2. Next, the problem is numerically modeled for a total of 175 (=5×5×7) possible settings of the design variables, and the different settings are compared on the basis of Pareto front concept by taking into account the above described four objective functions simultaneously.

Pareto front concept [31-33]:

In order to determine the best case (or series of best cases) from among 175 cases, "Pareto front concept" is used. In this concept, a case is said to be better than another, if it is better at least in one objective, and it is not worse in any other objective. In other words, "Solution A" is better than (or dominates) "Solution B", if:

Table 2. Convergence criteria (residuals) for the governing equations

Continuity	x-velocity	y-velocity	energy	k	ε	Do-intensity	species	NO
0.001	0.001	0.001	1e-08	0.001	0.001	1e-06	0.001	1e-06

$$N_{A,better} \geq 1 \quad and \quad N_{B,better} = 0 \tag{16}$$

Where, $N_{A,better}$ denotes the number of objective functions in which "solution *A*" is better than "solution B", and $N_{B,better}$ is the number of objective functions in which "solution *B*" is better than "solution *A*".

Moreover, solutions "*A*" and "*B*" are said to be non-dominant if none of them dominates the other one. If there is no solution better than a solution, that solution is said to be located on the Pareto front. It is worth noting that the solutions on the Pareto front are non-dominant (or they are not better than each other); therefore, each of them can be chosen as the optimal solution, depending on the designer's priorities. However, usually, among the solutions on Pareto front, the solution with the shortest distance from the ideal point is suggested as a trade-off or optimum case. The ideal point is an imaginary point whose each objective value is equal to the best value obtained from within all cases.

The previously mentioned terms are illustrated in Fig.4 for an imaginary problem in which two objective functions are to be minimized. As shown in Fig.4, solutions "*A*", "*B*", and "*C*" are located on the Pareto front, since there is no solution better than them. However, solutions "*D*" and "*E*" are not located on the Pareto front, because there is at least one solution better than them (solution "*A*" is better than solution "*D*", and solution "*B*" is better than solution "*E*"). Each of the solutions on the Pareto front ("*A*", "*B*", and "*C*") can be chosen as an optimum solution, depending on the designer's priorities. However, among them, solution "*B*" is the nearest one to the ideal point and is selected as the trade-off solution.

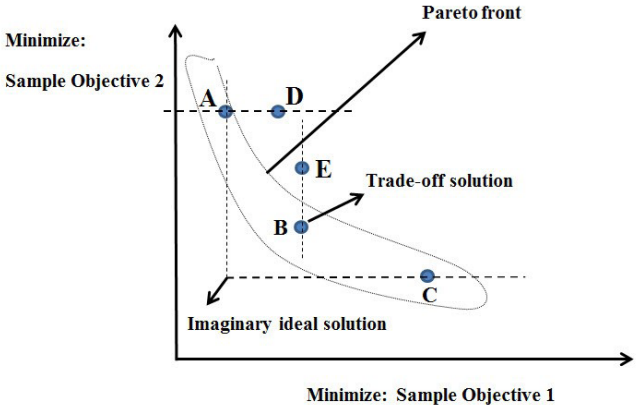

Fig. 4. Illustration of Pareto front terminology

4- Results and Discussion

In the following subsections, first, the results are presented in general terms. Then, the superiority of the modified design over the reference design is discussed in detail.

4- 1- Results in general terms

Fig. 5 shows the variations of the objective functions with respect to the design variables. The different designs (or different settings of design variables) are numbered on the basis of what is shown in Fig.6.

The noticeable variations of the objective functions with respect to the design number, shown in Fig.5, imply the substantial influence of the setting of the design variables. As shown in Figs. 5(a) and 5(b), the emissions of both CO and unburned CH_4 mostly increase by increasing L_2 and Φ. Fig. 5(c) indicates that the emission of NO increases with L_2, but it decreases with Φ. Also, Fig. 5(d) shows that the total heat transfer to the combustion chamber walls mostly decreases with both L_2 and Φ. However, the dependency of the objective functions to L_1 is not as explicit and obvious as the dependency of them to L_2 and Φ. It is worth noting that the mentioned trends are most likely to occur; however, the opposite trends are also observed in Fig.5.

Since four objectives are considered in this study, the Pareto front is 4-dimensional and can be presented with six two-dimensional plots, as shown in Fig. 7, where the triangles represent 21 cases located on Pareto front, and the circles represent the remaining cases.

Table 3 introduces trade-off design and shows that the trade-off design attained a noticeable improvement in each of the objective functions as compared to the reference design (previously described in section 2.2). In this study, thermal efficiency is defined as the ratio of the total heat transfer to the walls to the fuel heating rate (which is the product of the fuel mass flow rate and the fuel lower heating value). Since the fuel mass flow rate is kept constant for all designs, thermal efficiency is directly proportional to the heat transfer to the chamber walls.

4- 2- A detailed comparison of the reference and optimum cases

In this section, the reference and the modified cases are compared in detail. To gain some insight into the flame shapes, the temperature contours of the two cases are shown in Fig. 8. This figure indicates that the modified case led to a more uniform temperature distribution and lower peak temperature values as compared to the reference design.

Fig. 9 shows the rate of 1st reaction on some transverse lines at different axial locations, respectively. As shown in Fig. 9, in the modified case, the reaction began earlier and continued with lower rates at the end stages, as compared to the reference case.

Fig. 10 shows the convective, radiative, and total heat fluxes to the walls of the combustion chambers of the modified and reference cases. The mostly greater convective heat flux of the modified case than the reference case, shown in Fig. 10 (a), can be attributed to its higher air flow rate (Φ=1.3) compared to the reference case (Φ=0.95). However, the opposite trend is observed on a part of the front wall encircled

Table 3. Comparison of the optimum (or trade-off) and reference cases

design	L_1	L_2	φ	CH_4 at outlet gr/min	CO at outlet gr/min	NO at outlet gr/min	Thermal Efficiency (%)
Trade-off	2.5	1	1.3	7.53E-01	3.74E+00	4.09E-05	50.97
Reference	3	2	0.95	4.71	19.9	3.58E-03	39.38
Improvement (%)	-	-	-	83.9	81.2	98.6	29.4

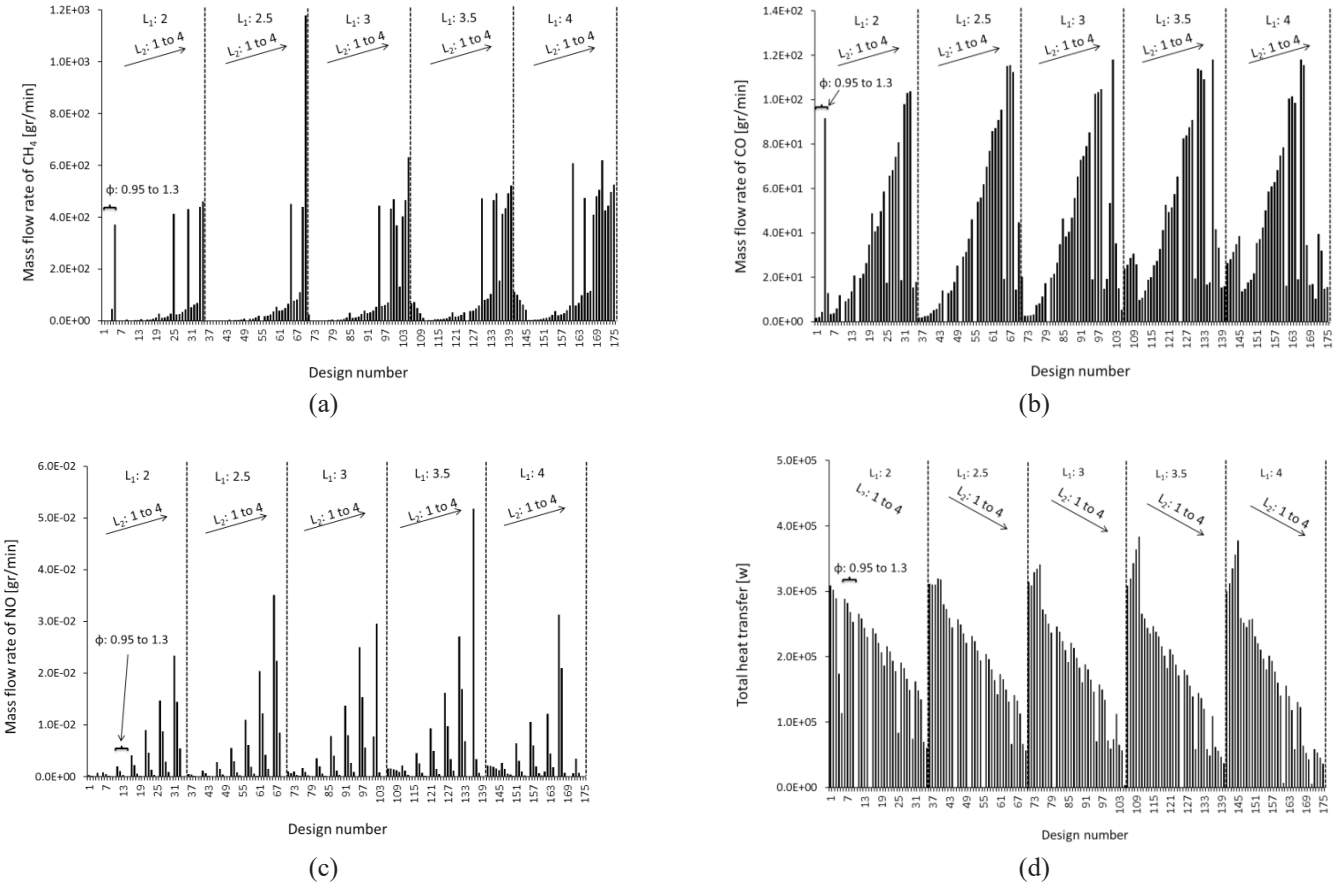

Fig. 5. Variations of (a) emission of CH4 (b) emission of CO (c) emission of NO (d) total heat transfer with respect to the setting of design variables

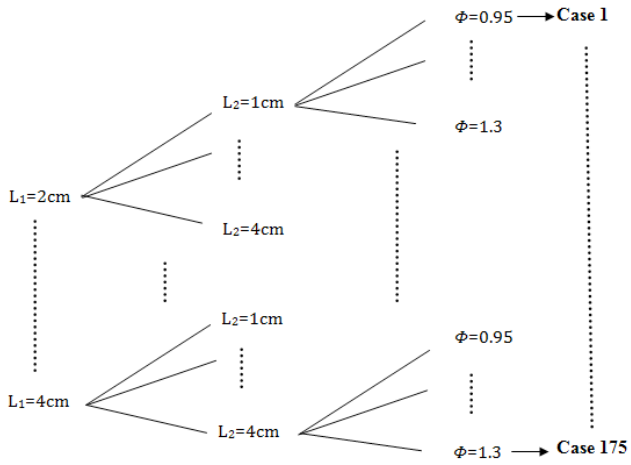

Fig. 6. Design (case) numbering

in Fig. 10 (a). This observation resulted from the more direct flame impingement of the reference case in that region as compared to the modified case. Total convective heat transfer rates are 93.5kW and 173.8kW for the reference and modified cases, respectively. As shown in Fig. 10 (b), the more uniform temperature distribution of the modified case led to a more uniform radiative heat flux to the walls. However, the hot spots of the reference case at the end stages of the chamber resulted in its 5.4% higher total radiative heat transfer rate as compared to the modified case. Total radiative heat transfer rates are 152.4kW and 144.6kW for the reference and the modified cases, respectively. The total heat flux curve (i.e., the sum of convective and radiative heat fluxes) shown in Fig. 10 (c) indicates that the modified case led to a greater heat flux on the back and side walls; however, the total heat flux to the front wall is approximately the same for the two cases. As previously shown in Table 3, the modified case resulted in a 29.4% greater total heat transfer rate as compared to the reference case.

Fig. 11 shows the molar concentration of methane on the centerline. As shown in this figure, the curve of the modified case lies below that of the reference case. This is because the air OER of the modified case is higher than that of the reference case; moreover, in the modified case, the beginning of reactions takes place nearer to the inlets. Therefore, the modified case shows a lower value of unburned methane at the exhaust as compared to the reference case.

Although the creation or the consumption of each species depends on several local variables, air deficiency of the reference case (OER=0.95) may be a reason for its higher emission of CO as compared to the modified case, previously shown in Table 3. Fig. 12 shows the molar concentration of CO on some transverse lines at different axial locations. This figure indicates that in the modified case, CO began to be created earlier, and therefore, it had a longer residence time to be consumed by the combustion chamber. This observation may be considered as another reason for the higher emission of CO in the reference case as compared to the modified one.

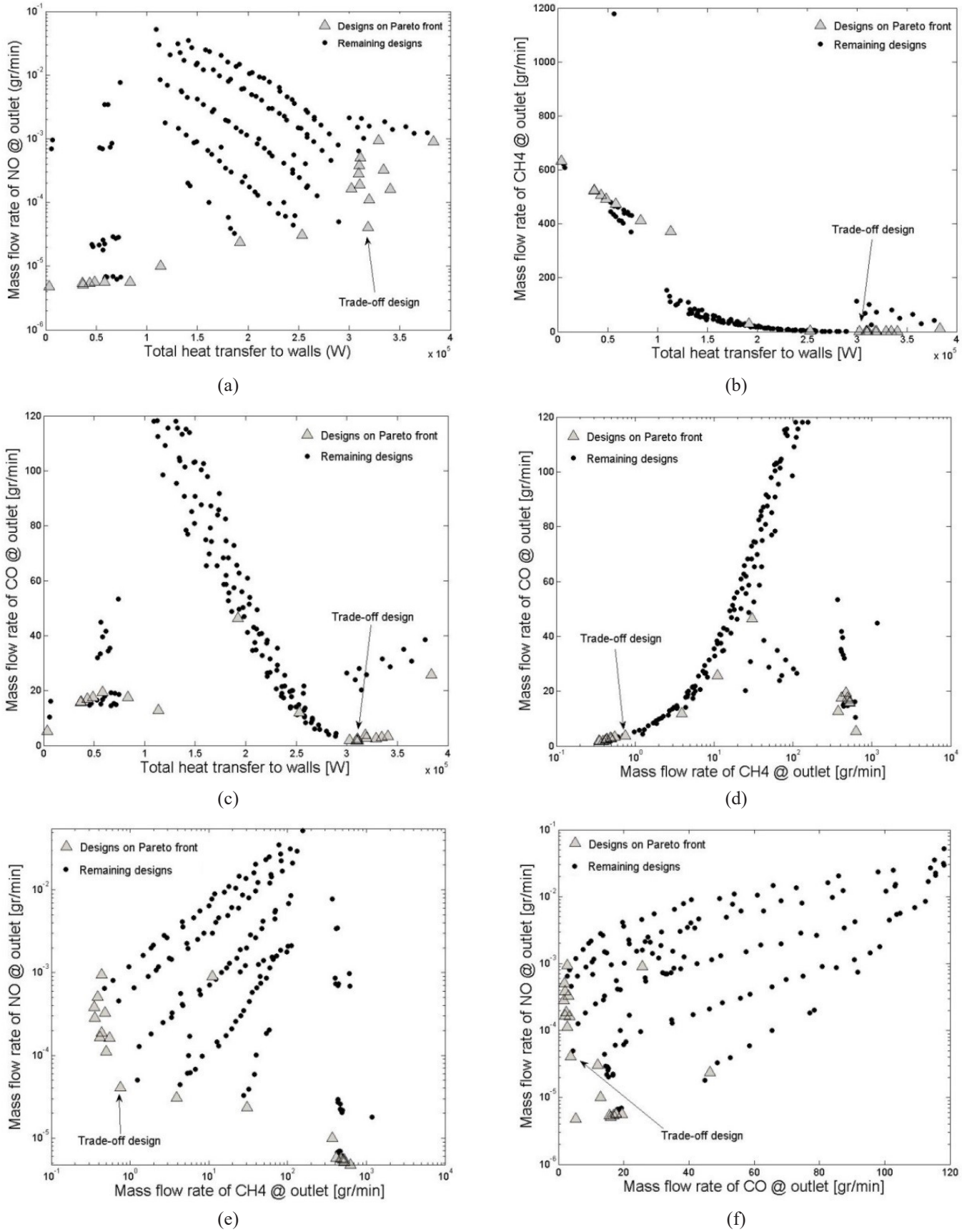

Fig. 7. 2-D presentation of Pareto front (a) NO-Heat transfer (b) CH4- Heat transfer (c) CO-Heat transfer (d) CO-CH4 (e) NO- CH4 (f) NO-CO

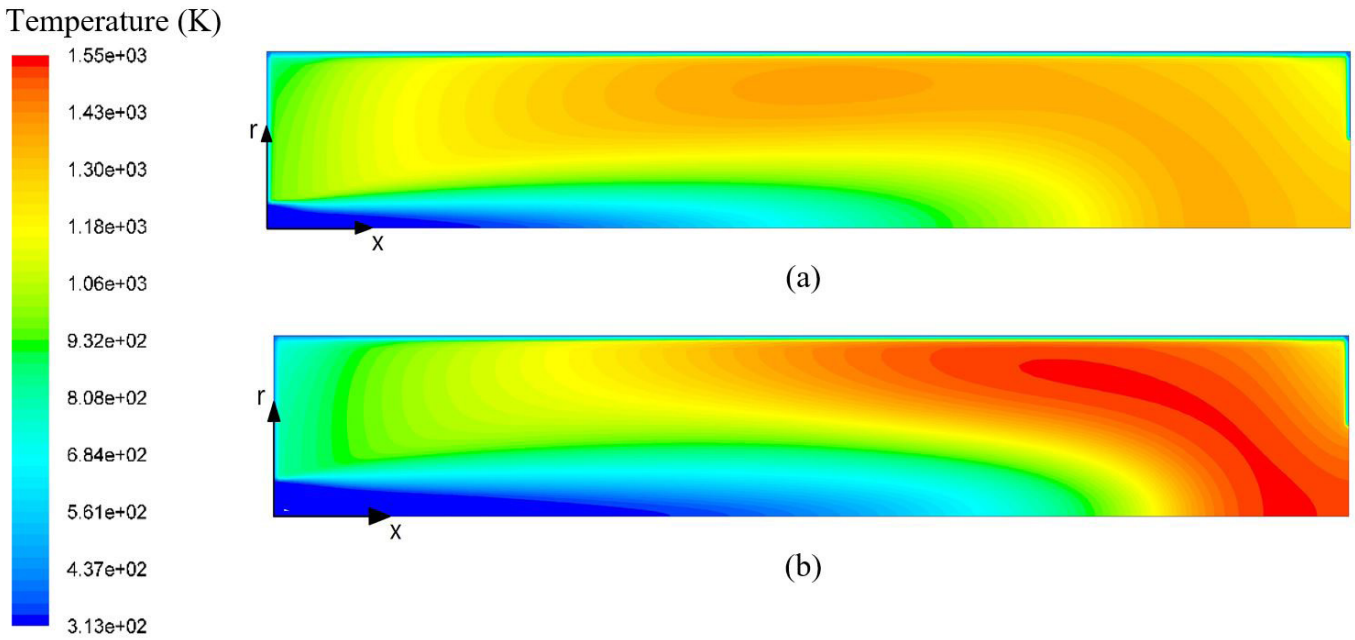

Fig. 8. Contours of temperature for (a) optimum case (b) Reference case

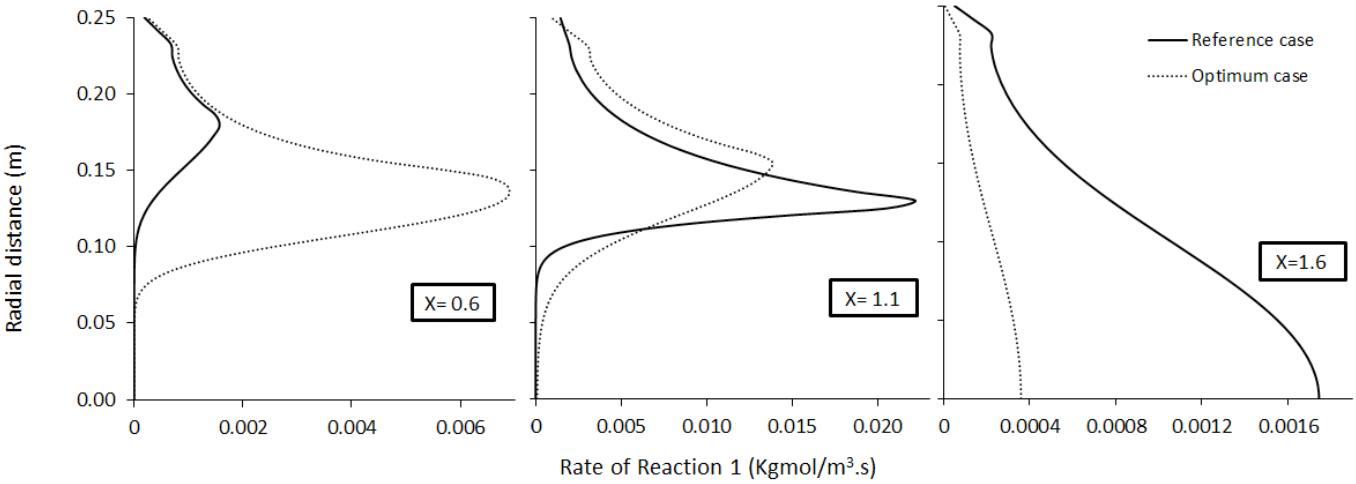

Fig. 9. The rate of reaction on some transverse lines at different axial locations

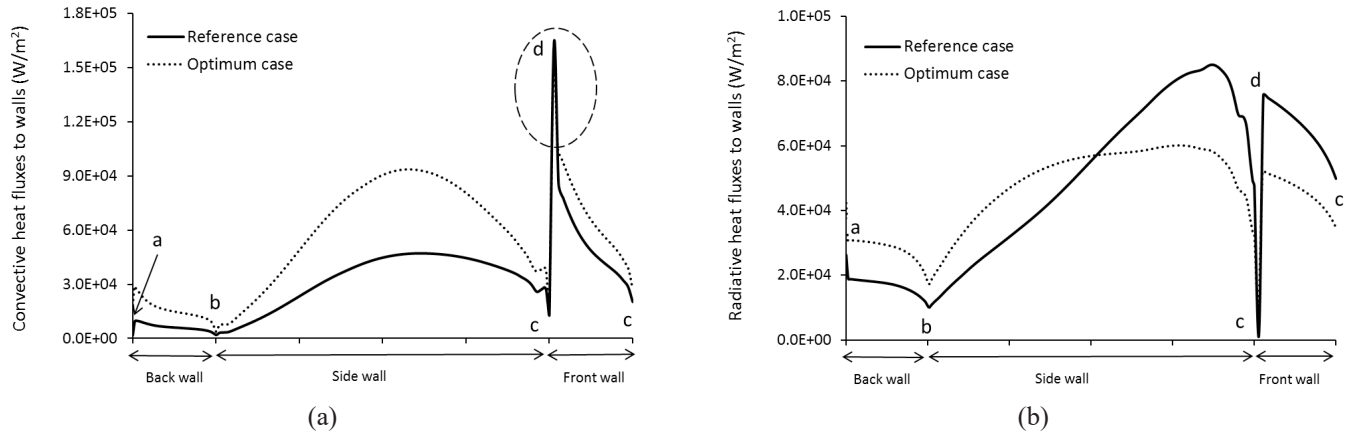

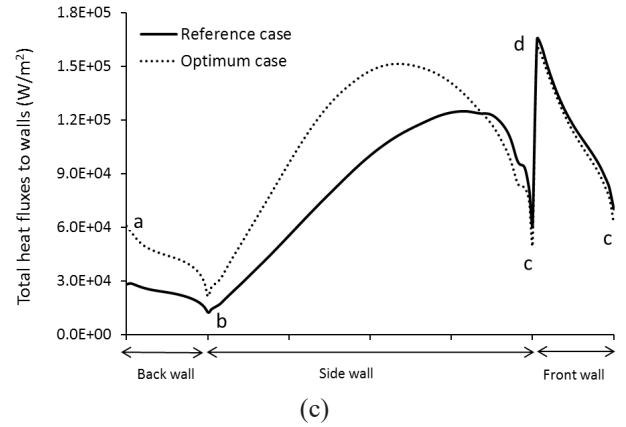

(c)

Fig. 10. (a) Convective (b) radiative (c) total heat transfer to the walls

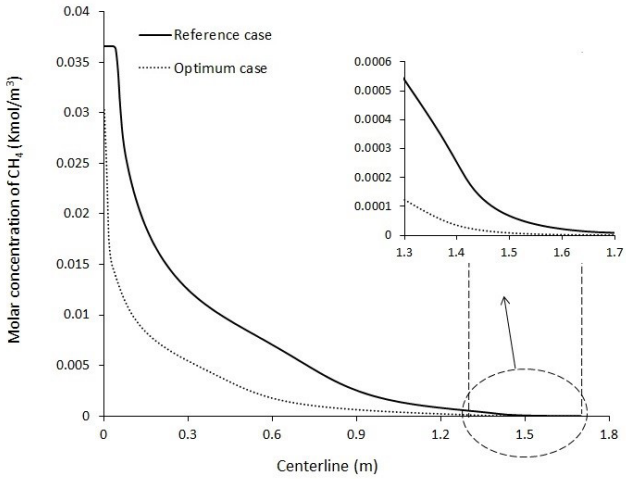

Fig. 11. The molar concentration of CH4 on the centerline

The results show that the rate of prompt NO is much higher than that of thermal NO (that is not shown here for the sake of conciseness). This is usually the case for low-temperature flames [23, 28]. The rates of prompt NO formation on the centerline of the reference and modified cases are compared in Fig. 13 (a). This Figure shows that the modified case led to the substantially lower rates of prompt NO. As shown in Eq. (15), prompt NO formation non-linearly depends on several local variables (i.e., local O_2, N_2 and fuel concentrations, and local temperature). Among the mentioned factors, the fuel (CH_4) concentration curves were previously shown in Fig. 11. Herein, the variations of temperature and concentrations of N_2 and O_2 are presented in Figs. 13 (b) to (d).

The two vertical lines in Figs. 11 and 13 highlight the limit within which the differences between NO formations of the modified and reference cases are more considerable. Fig. 13 shows that the curve lines of the modified and reference cases intersect for each of the temperature, O_2, and N_2 concentrations. In other words, the values of temperature, O_2 and N_2 concentrations of the modified case are higher somewhere, but lower somewhere else, as compared to those of the reference case. However, as shown in Fig. 11, the fuel concentration of the modified case with the air to fuel OER of 1.3 is always lower than that of the reference case with the air to fuel OER of 0.95. As a result, the higher prompt NO formation of the reference case can be primarily attributed to its higher fuel concentrations.

5- Conclusions

In the present work, it was attempted to reach better thermal and environmental characteristics of a natural gas diffusion flame through the numerical examination of the various settings of air to fuel overall equivalence ratio (OER) and the sizes of fuel and air inlets. The selection of optimal design was performed on the basis of Pareto front concept by considering four thermal and environmental objective functions. The results indicated that:

- The emissions of pollutants mostly increased with both air inlet size and air to fuel OER, except that the emission of NO decreased with air to fuel OER. Moreover, the total heat transfer mostly decreased with both air inlet size and air to fuel OER. The dependency of the objectives to the fuel inlet size was not as explicit and obvious as the dependency of them to the air inlet size and OER.
- From among 175 numerically tested designs, 21 designs were located on Pareto front, each of which could be chosen as the optimum case depending on designer's

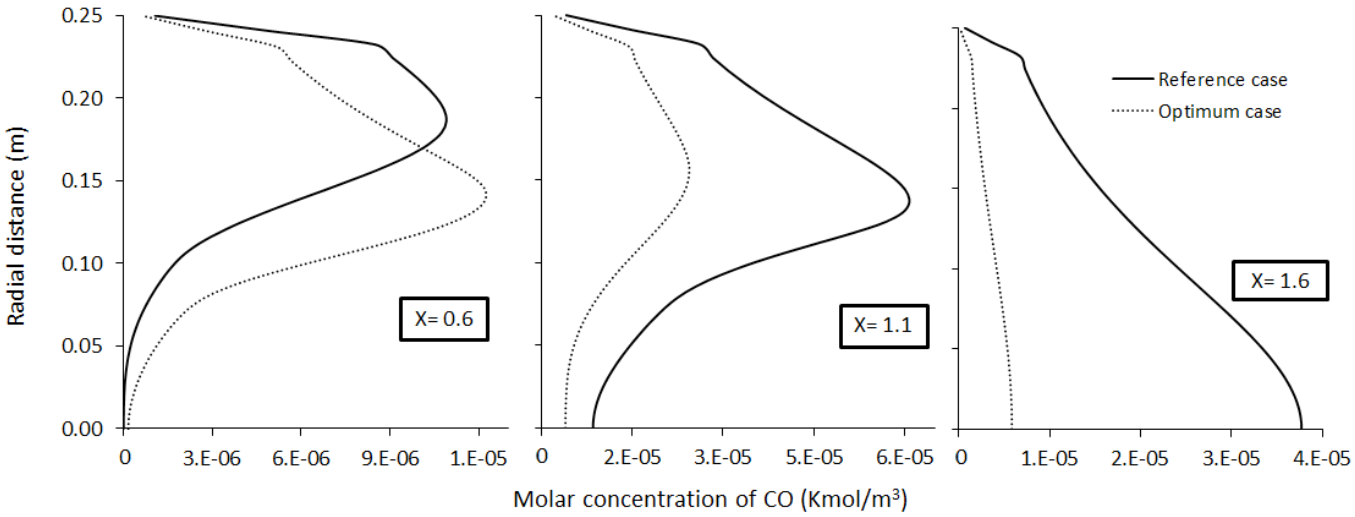

Fig. 12. The molar concentration of CO on some radial lines at different axial locations

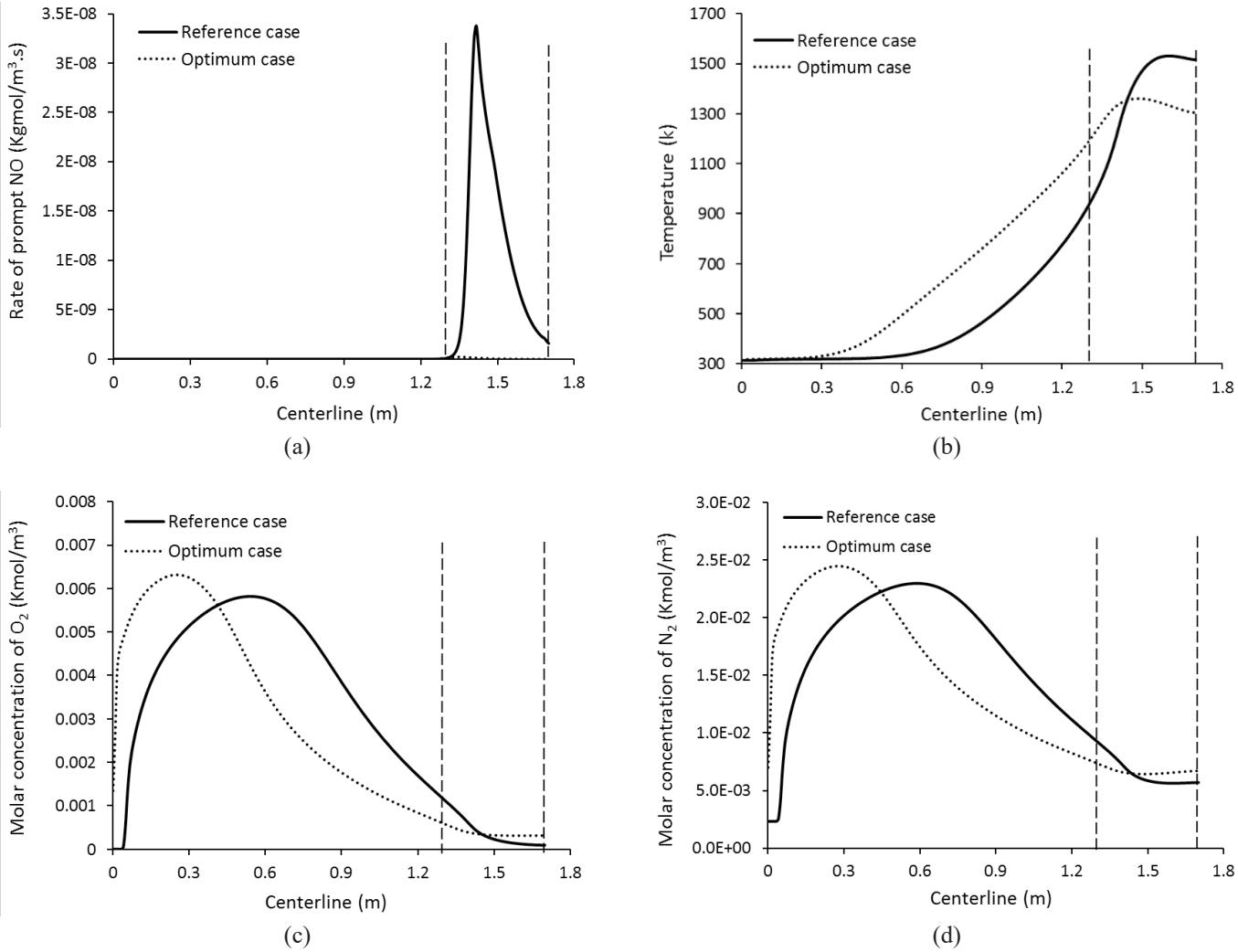

Fig. 13. Comparison of (a) prompt NO (b) temperature (c) molar concentration of O_2 (d) molar concentration of N_2 on the centerlines of the optimum and reference cases

priorities.

- The selected trade-off (optimum) design attained a noticeable improvement in each of the objective functions as compared to the reference design.
- The reference design showed a higher peak temperature and, hence, a little greater radiative heat transfer; however, the optimum design attained noticeably higher total heat transfer due to its substantially higher convective heat transfer.
- The lower emissions of CO and unburned CH_4 of the optimum design was attributed to its higher air to fuel OER as well as its earlier beginning of the reactions providing a longer residence time for the CH_4 and CO to be consumed inside the combustion chamber.
- The lower NO formation of the optimum case was attributed to its lower fuel concentrations (or leaner flame).

Acknowledgments

Guilan Province Gas Company is gratefully acknowledged for supporting this study (contract No 31548).

Nomenclature

A	Constant
Ar	Pre-exponential factor, Consistent unit
a	Absorption coefficient, m^{-1}
B	Constant
C_p	Heat capacity at constant pressure, $J.kg^{-1}.K^{-1}$
D	Diffusion coefficient, $m^2.s^{-1}$
E	Activation energy, $J.kgmol^{-1}$
E'_d	Constant, $J.kgmol^{-1}$
f	Constant
g	Oxygen reaction order
h	Enthalpy, $J.kg^{-1}$
I	Radiation intensity, $W.m^{-2}$
K	Thermal conductivity, $W.K^{-1}.m^{-1}$
k	Rate constant, $m^3.gmol^{-1}.s^{-1}$
L_1	Dimension of fuel inlet, m
L_2	Dimension of the air inlet, m

M	Molecular weight, kg.mol^{-1}
N	Number of chemical species
n	Refractive index
Pr	Prandtl number
p	Pressure, Pa
R_k	Rate of creation, Kmol.m^{-3}s^{-1}
R	Universal gas constant, J.kgmol^{-1}.K^{-1}
r	Position vector
s	Direction vector
s'	Scattering direction
Sc	Schmidt number
T	Temperature, K
u	Velocity, m.s^{-1}
Y	Mass fraction

Greek symbols

β	Constant
η	Thermal efficiency
μ	Viscosity, kg.m^{-1}.s^{-1}
v'	stoichiometric coefficient for reactant
v''	stoichiometric coefficient for product
ρ	Density, kg.m^{-3}
σ	Stefan- Boltzmann constant, W.m^{-2}.K^{-4}
σ_s	scattering coefficient, m^{-1}
φ	Equivalence ratio
Ω'	solid angle, Radians

Subscript

f	Forward reaction
k	chemical species
p	Product
R	Reactant
r	Backward reaction
t	Turbulent

References

[1] International Energy Agency (IEA), *Key World Energy Statistics*, OECD, Paris, 2016.

[2] J. Mahmoudimehr, L. Loghmani, Optimal management of a solar power plant equipped with a thermal energy storage system by using Dynamic Programming method, Proceedings of the Institution of Mechanical Engineers, *Part A: Journal of Power and Energy*, 230 (2) (2016) 219-233.

[3] N. Papanikolaou, I. Wierzba, The effects of burner geometry and fuel composition on the stability of a jet diffusion flame, *Journal of Energy Resources Technology*, 119 (4) (1997) 265-270.

[4] A. Sobiesiak, J.C. Wenzell, Characteristics and structure of inverse flames of natural gas, *Proceedings of the Combustion Institute*, 30 (1) (2005) 743-749.

[5] L.K. Sze, C.S. Cheung, C.W. Leung, Appearance, temperature and NOx emission of two inverse diffusion flames with different port design, *Combustion and Flame*, 144 (1) (2006) 237–248.

[6] P. Hariharan, C. Periasamy, S.R. Gollahalli, Effect of elliptic burner geometry and air equivalence ratio on the nitric oxide emissions from turbulent hydrogen flames, *International Journal of Hydrogen Energy*, 32 (8) (2007) 1095–1102.

[7] U. Makmool, S. Jugjai, S. Tia, P. Vallikul, B. Fungtammasan, Performance and analysis by particle image velocimetry (PIV) of cooker-top burners in Thailand, *Energy*, 32 (10) (2007) 1986–1995.

[8] F. Liu, G.J. Smallwood, Control of the structure and sooting characteristics of a co-flow laminar methane/air diffusion flame using a central air jet: an experimental and numerical study, *Proceedings of the Combustion Institute*, 33 (1) (2011) 1063–1070.

[9] L.L. Dong, C.S. Cheung, C.W. Leung, Combustion optimization of a port-array inverse diffusion flame jet, *Energy*, 36 (5) (2011) 2834-2846.

[10] L.L. Dong, C.S. Cheung, C.W. Leung, Heat transfer optimization of an impinging port-array inverse diffusion flame jet, *Energy*, 49 (1) (2013) 182-192.

[11] L.L. Dong, C.S. Cheung, C.W. Leung, Characterization of impingement region from an impinging inverse diffusion flame jet, *International Journal of Heat and Mass Transfer*, 56 (1-2) (2013) 360–369.

[12] H.S. Zhen, Y.S. Choy, C.W. Leung, C.S. Cheung, Effects of nozzle length on flame and emission behaviors of multi-fuel-jet inverse diffusion flame burner, *Applied Energy*, 88 (9) (2011) 2917–2924.

[13] O.A. Kashkousha, M.M. Kamal, A.M. Abdulaziz, M.A. Nosier, Concentric elliptical jet diffusion flames with co- and cross-flows, *Experimental Thermal and Fluid Science*, 41 (2012) 177–187.

[14] S. Mahesh, D.P. Mishra, Effects of recessed air jet on turbulent compressed natural gas inverse diffusion flame shape and luminosity, Combustion, *Explosion and Shock Waves*, 48 (6) (2012) 683–688.

[15] S. Mahesh, D.P. Mishra, Flame stability limits and near blowout characteristics of CNG inverse jet flame, *Fuel*, 153 (2015) 267–275.

[16] S. Lamige, J. Min, C. Galizzi, F. André, F. Baillot, D. Escudié, K.M. Lyons, On preheating and dilution effects in non-premixed jet flame stabilization, *Combustion and Flame*, 160 (6) (2013) 1102–1111.

[17] H.S. Zhen, C.W. Leung, T.T. Wong, Improvement of domestic cooking flames by utilizing swirling flows, *Fuel*, 119 (1) (2014) 153–156.

[18] M. Saediamiri, M. Birouk, J.A. Kozinski, On the stability of a turbulent non-premixed biogas flame: Effect of low swirl strength, *Combustion and Flame*, 161 (5) (2014) 1326–1336.

[19] M. Akbarzadeh, M. Birouk, Liftoff of a Co-Flowing Non-Premixed Turbulent Methane Flame: Effect of the Fuel Nozzle Orifice Geometry, Flow, *Turbulence and Combustion*, 92 (4) (2014) 903–929.

[20] M. Saediamiri, M. Birouk, J.A. Kozinski, Enhancing the Stability Limits of Biogas Non-Premixed Flame, *Combustion Science and Technology*, 188 (11-12) (2016) 2077-2104.

[21] P. Kuntikana, S.V. Prabhu, Thermal investigations on methane-air premixed flame jets of multi-port burners, *Energy*, 123 (2017) 218-228.

[22] I. Bonefacic, I. Wolf, P. Blecich, Improvement of fuel oil spray combustion inside a 7 MW industrial furnace: A numerical study, *Applied Thermal Engineering*,110 (2017) 795–804.

[23] C.K. Law, *Combustion Physics*, Cambridge University Press, New York, 2006.

[24] N. Peters, *Turbulent Combustion*, Cambridge University Press, Cambridge, 2000.

[25] B.F. Magnussen, B.H. Hjertager, On mathematical modelling of turbulent combustion with special emphasis on soot formation and combustion, *Proceedings of the 16th symposium (international) on combustion*, (1976) 719–729.

[26] H.C. Hottel, A.F. Sarofim, *Radiative Transfer*, McGraw-Hill, New York, 1967.

[27] R. Siegel, J.R. Howell, *Thermal Radiation Heat Transfer*, Taylor and Francis, Washington, 1992.

[28] J. Warnatz, U. Mass, R.W. Dibble, *Combustion*, Springer, Berlin, 2006.

[29] S.V. Patankar, *Numerical Heat Transfer and Fluid Flow*, McGraw-Hill, New York, 1980.

[30] D. Garréton, O. Simonin, *Aerodynamics of steady state combustion chambers and furnaces*, ASCF. Ercoftac Cfd Workshop, Org: EDF Chatou, France, 1994.

[31] F. Hajabdollahi, Z. Hajabdollahi, H. Hajabdollahi, Soft computing based multi-objective optimization of steam cycle power plant using NSGA-II and ANN, *Applied Soft Computing* 12 (11) (2012) 3648-3655.

[32] K. Deb, *Multi objective optimization using evolutionary algorithms*, Wiley, New York, 2001.

[33] C.A. Coello, G.B. Lamont, D.A.Van Veldhuizen, *Evolutionary algorithms for solving multi-objective problems*, Springer, New York, 2002.

Please cite this article using:

S. F. Mousavi Kolousforoushi and J. Mahmoudimehr, Influence of Burner Head Design on Its Thermal and Environmental Characteristics, *AUT J. Mech. Eng.*, 2(1) (2018) 27-38.

DOI: 10.22060/mej.2017.13172.5561